Tailoring cathode materials: A comprehensive study on LNMO/LFP blending for next generation lithium-ion batteries

Journal of Power Sources 613 (2024) 234955

Contents lists available at ScienceDirect

Journal of Power Sources

journal homepage: www.elsevier.com/locate/jpowsour

Tailoring cathode materials: A comprehensive study on LNMO/LFP blending for next generation lithium-ion batteries

Daniele Versaci [a,*], Roberto Colombo [a], Giorgio Montinaro [a], Mihaela Buga [b], Noelia Cortes Felix [c], Gary Evans [c], Federico Bella [a], Julia Amici [a], Carlotta Francia [a], Silvia Bodoardo [a]

[a] Politecnico di Torino, Department of Applied Science and Technology, Electrochemistry Group, Corso Duca Degli Abruzzi, 24, 10129, Turin, Italy
[b] National Research and Development Institute for Cryogenic and Isotopic Technologies Rm. Valcea, ICSI ENERGY Department, 4 Uzinei, 240050, Ramnicu Valcea, Romania
[c] Johnson Matthey Technology Centre, Blounts Court, Sonning Common, Reading, RG4 9NH, United Kingdom

HIGHLIGHTS

- Resonant acoustic mixing improves the LFP distribution on LNMO particle's surface.
- LFP addition to LNMO increases the electrochemical performance of the cathode.
- Low amount of LFP (2 wt%) improves the capacity retention in half and full-cell.
- LFP compensates the lithium loss during cycling, acting as lithium donor.
- Blended LNMO/LFP exhibits a capacity retention >80 % after 1000 cycles at 1C.

GRAPHICAL ABSTRACT

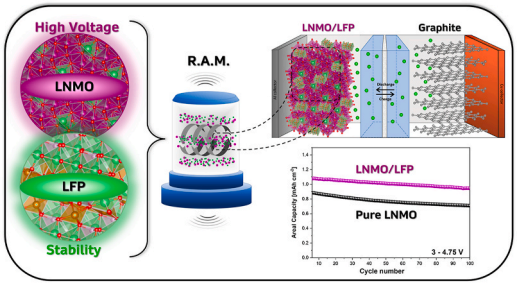

ARTICLE INFO

Keywords:
Lithium-ion batteries
Cathode materials
LNMO/LFP blended cathode
Energy density
Cycling stability

ABSTRACT

Lithium-ion batteries (LIBs) play a crucial role in diverse applications, including electric vehicles, portable electronics, and grid energy storage, owing to their commendable features, such as high energy density, extended cycle life, and low self-discharge rates. Despite their widespread use, the growing market demands continuous efforts to enhance LIBs performance, particularly in terms of energy density and cycling stability. This paper details the development of a lithium nickel manganese oxide (LNMO - $LiNi_{0.5}Mn_{1.5}O_4$)/lithium iron phosphate (LFP - $LiFePO_4$) blended cathode for high-performance LIBs. The study investigates the impact of blending LFP and LNMO, examining morphological and electrochemical aspects. The usage of resonant acoustic mixing (RAM) technology is demonstrated to be a promising approach to improve the distribution of LFP and LNMO particles, leading to increased electrochemical performance. The blended LNMO/LFP cathode exhibits a specific capacity exceeding 125 mAh g^{-1} at C/10 and a capacity retention exceeding 80 % after 1000 cycles at 1C versus lithium. Moreover, in a full-cell configuration, the blended electrode displays a capacity retention close to 74 % after 100 cycles, showcasing a nearly 30 % improvement compared to the pure LNMO cathode. This research highlights the potential of blended cathode materials in advancing the capabilities of LIBs.

* Corresponding author.
E-mail address: daniele.versaci@polito.it (D. Versaci).

https://doi.org/10.1016/j.jpowsour.2024.234955
Received 24 February 2024; Received in revised form 30 May 2024; Accepted 20 June 2024
Available online 24 June 2024

1. Introduction

In pursuing of more efficient and advanced energy storage solutions, lithium-ion (LIBs) batteries have emerged as a crucial technology powering a wide range of applications, from portable electronics to electric vehicles. Central to the performance and overall capabilities of LIBs is the electrode active material, which plays a decisive role in the battery electrochemical processes. For this reason, over the years, extensive research has been devoted to synthesize and enhance the active materials in order to improve some fundamental aspects of the Li-ion cell, such as energy density, cycling stability, and safety [1]. The study of various cathode materials with different crystalline structures, predominantly layered, olivine and spinel ones, has been at the centre of attention, in order to develop materials that combine high electrochemical performance and a greater degree of environmental sustainability. Each category of active materials exhibits specific properties that render them suitable in lithium-ion batteries. However, these materials are also affected by certain limitations and challenges that currently limit the identification of a singular 'perfect' cathode material [2]. In recent years, even at a commercial level [3], a different approach has been applied to achieve more versatile and high-performance batteries, involving the combinations of various cathode materials. The primary goal in blending different cathode materials is to exploit their characteristic properties while simultaneously mitigating the drawbacks of each individual component [4]. In this way, individual limitations of the materials can be potentially overcome and the overall performance of the cathode can be synergistically enhanced. For instance, by incorporating complementary components, the resulting blended material may demonstrate improved electrochemical properties, higher energy density, and enhanced cycling stability. This kind of approach allows for the customization of Li-ion battery characteristics to meet specific application requirements. Within this framework, various combinations and ratios of active materials can be explored, rendering blended cathodes highly adaptable and suitable for a spectrum of applications, from small-scale portable devices to large-scale energy storage systems. In recent times, numerous investigations have focused on blended cathodes, combining commonly used active materials such as lithium nickel manganese cobalt oxide (NMC), lithium nickel cobalt aluminium oxide (NCA), lithium manganese oxide (LMO), lithium manganese iron phosphate (LFMP), etc. [5–14]. Most of these studies investigated the combination of spinel lithium manganese oxide (LMO) with layered oxide such as NMC [15–19] and NCA [20]. Alternatively, Al-doped LMO was also combined with olivine active materials such as lithium manganese iron phosphate (LMFP) by Klein et al. [12,13]. Analogously, layered NMC was blended with olivine cathode such as LFP [21] by Gallagher et al. [22], while regarding high voltage spinel (LNMO), to the best of our knowledge, only Cai et al. [9] reported the investigation of this material in a blended formulation, combining it with LCO. Recently, the group of Michaelis deeply investigated the combination of different cathode materials mixed by physical blending: LMO + LFP [4,5,23], LMO + NMC [4,5], LCO + LFP [10,11], underlining the need to study blended systems to better understand the interaction between different materials and their synergistic effect. However, in many cases, as also reported by other studies, the beneficial effects derived from blending cathode materials remain not well understood, necessitating further efforts and optimization processes in the mixing procedure and electrode design [8,18,19].

Nowadays, there has been a particular emphasis on cathode materials that are environmentally friendly, entirely cobalt-free, and cost-effective, such as LNMO (spinel) and LFP (olivine). However, despite their undeniable advantages, both materials exhibit certain drawbacks that limit their application in specific scenarios. On one hand, LNMO (lithium nickel manganese oxide – $LiNi_{0.5}Mn_{1.5}O_4$) operates at high voltage (e.g., 4.75 V vs. Li/Li^+) with a theoretical specific capacity of 147 mAh g^{-1}, making it particularly interesting for enhancing the electrochemical performance of next-generation high-energy-density LIBs. Unfortunately, LNMO still suffers from some disadvantages such as cation leaching during cycling and electrolyte decomposition at high voltage, which inevitably reduce the safety of the system, limiting the practical application of this material [2,24–26]. On the other hand, LFP stands out as a safer and more stable cathode material, exhibiting high thermal stability and a longer cycle life. LFP resistance to degradation over repeated charge-discharge cycles makes it attractive for addressing safety concerns. Unfortunately, while LFP has a theoretical specific capacity of 175 mAh g^{-1}, its operating voltage of 3.4 V vs. Li/Li^+, results in lower energy density. This characteristic inevitably makes LFP less suitable for applications with high energy requirements [2,27].

Starting from these considerations, blending LNMO and LFP offers the potential to achieve a balance between high energy density and stable cycle life, making their combination a suitable solution for developing the next generation of LIBs.

Despite these premises, the study of blended materials combining LNMO with LFP has received limited attention. To the best of our knowledge, aside from some works where a layer of $FePO_4$ or LFP has been applied to LNMO particles [28–32], the physical mixing of these two materials has not been thoroughly explored.

Hence, the objective of this study is to investigate the electrochemical properties of blended LNMO/LFP cathodes, obtained by physically mixing the two materials adopting the resonant acoustic mixing (RAM) technique. The effect of blending LNMO with two different LNMO/LFP ratios was assessed using both half-cell and full-cell configurations, in order to deeply study the role of the LFP when combined with LNMO. The influence of each component on the electrochemical performance was systematically examined using various techniques, correlating the results with the structural and morphological aspects of the electrodes. It is important to highlight that, based on the authors' knowledge, the study and comparison of the effect of mixing cathode materials in both configurations, particularly in full-cell, is still lacking in the scientific literature. As a matter of fact, the application of this type of blended cathode in full-cell, *i.e.* in more realistic and practical conditions, is essential to elucidate the role of the different components within the cathode.

2. Material and methods

2.1. Preparation of blended LNMO/LFP cathode materials

$LiNi_{0.5}Mn_{1.5}O_4$ (LNMO) and $LiFePO_4$ (LFP, carbon coated) used in the present study were provided by Johnson Matthey. Blending of the two cathode materials was carried out using a LabRAM I ResonantAcoustic Mixer (Resodyn Acoustic Mixers). The resonant frequency was automatically adjusted to 60–61 Hz, for 5 min with an acceleration value of 100 g's.

2.2. Chemico-physical characterization of blended LNMO/LFP cathode materials

The Brunauer-Emmett-Teller (BET) specific surface area (SSA) was determined by nitrogen physisorption at 77 K using AUTOSORB-1-C (Quantachrome).

X-ray diffraction (XRD) analysis was carried out by a PANalytical X'Pert (Cu Ka ra-diation) diffractometer. Data were collected with a 2D solid state detector (PIXcel) from 10 to 80° 2θ with a step size of 0.026 2θ and a wavelength of 1.54187 °A.

Field emission scanning electron microscopy (FESEM) analysis was carried out by Zeiss SUPRA TM 40 with Gemini column and Schottky field emission tip (tungsten at 1800 K). Acquisitions were made at an acceleration voltage of 3 kV and working distance within 2.1–8.5 mm, with magnification up to 150 kX.

2.3. Electrochemical characterization of LNMO/LFP cathode

All the electrodes were prepared by solvent tape casting method. The cathode slurry was prepared by mixing 90 wt% of active material (pure or blended), 5 wt% of conducting carbon black (TIMCAL C-NERGYTM Super C65, ImerysCarb.), and 5 wt% of binder poly (vinylidene fluoride) (PVdF - HSV900) solution, (10 wt% in N-methyl pyrrolidone - NMP). After complete binder dissolution, carbon black and active material were added and the slurries were homogenized using a ball mill for 15 min at 30 Hz.

All the slurries were cast on carbon-coated aluminium foil (ARMOR Group, 19.8 μm-thick, and 1.1 μm-carbon thick) using a doctor blade (adjusted for a 300 μm-thick deposition) and an automatic film applicator (Sheen 1133 N) with a speed of 50 mm s^{-1}.

After evaporating the solvent at 50 °C for 1 h, electrode disks with an area of 0.785 and 1.766 cm^2 were punched out and vacuum dried at 120 °C (Büchi Glass Oven B-585) for 4 h, then transferred into an argon filled dry glove box (MBraun Labstar, H_2O and O_2 content <1 ppm) for the half-cell and full-cell assembly. The final mass loading of the LNMO-based dried electrodes was in the range of 10.5–11.5 mg cm^{-2}. For a better comparison, a pure-LFP electrode was prepared using the same formulation and a similar mass loading.

Three-electrode cyclic voltammetry tests were carried out with a Swagelok-type T-cell using lithium disks (Ø 10 mm, 0.3 mm-thick, high purity lithium foils, Chemetall Foote Corp.) as counter and reference electrodes, in the potential range of 3–4.9 V at RT with a fixed scan rate of 0.1 mV s^{-1} or at different scan rates (*i.e.,* 0.1, 0.2, 0.3, 0.4 and 0.5 mV s^{-1}).

The cycling performances (rate capability and capacity retention test), in half and full configuration, were investigated by assembling 2032-type coin cells, using lithium disks (Ø 16 mm, 0.6 mm-thick, Tobmachine) or graphite anode (PE16, Elkem) as counter and reference electrode, respectively. All galvanostatic charge-discharge cycling tests were carried out using an Arbin BT-2000 battery tester at room temperature, in the potential range of 3–4.9 V vs. Li/Li^+ for half-cell configuration and 3–4.75 V for full-cell configuration. The charge/discharge rates were based on the LNMO theoretical specific capacity of 147 mAh g^{-1}.

The galvanostatic intermittent titration technique (GITT) was used on half cells to investigate the overpotential and the variation of the lithium-ion diffusion coefficient within the cathode materials examined in this study as a function of the state of charge of the cell. In particular, the protocol consisted of three training cycles at a C-rate of 0.1C, followed by a GITT discharge and charge cycle in which a current pulse at 0.1C was applied for 10 min, followed by a relaxation time of 2 h. Both training cycles and GITT were performed in the potential range of 3–4.9 V.

To better evaluate the overall resistance inside the cells, potentiostatic electrochemical impedance spectroscopy (PEIS) measurements were carried out by a versatile multichannel potentiostat (VMP-3 Biologic). Impedance measurements were performed at different state of charge (SOC) using an amplitude of 10 mV in the frequency range of 500 kHz to 50 mHz.

Three-electrode cycling performances were evaluated using a PAT-Cell (EL Cell) by a versatile multichannel potentiostat (VMP-3 Biologic) using graphite as counter electrode and lithium ring as reference. The three-electrodes cell configuration was used to control and deconvolute the voltage profiles of the anode and cathode during charge and discharge process.

For all the electrochemical tests, the electrolyte was a solution of $LiPF_6$ 1.0 M dissolved in a mixture 1:1 v/v of ethylene carbonate (EC) and diethyl carbonate (DEC) + 5 % fluoroethylene carbonate (FEC), provided by Solvionic, soaked on a glass fibre separator (Whatman GF/A; 0.63 mm-thick). All studies were performed at room temperature (25 °C).

3. Results and discussion

3.1. LNMO/LFP structural and morphological characterization

To achieve a uniform and homogeneous mixing, resonant acoustic mixing was employed to blend the two cathode materials (*i.e.,* LNMO and LFP). RAM was selected as the mixing technique because it is an innovative and scalable method that enables homogeneous mixing in a short time and with low energy costs [33–35]. Two LFP additive loadings were considered: 2 wt% and 10 wt%, respectively named LNMO +2 % LFP and LNMO +10 % LFP (Table 1).

Following the mixing process, the morphology of the blended samples was assessed through FE-SEM and energy-dispersive X-ray spectroscopy (EDX) analyses, and the results were compared with those of the pure materials, as reported in Fig. 1.

The FE-SEM micrographs of the individual powders show the typical octahedral-like particles arranged in agglomerations of various sizes (from 1 to 100 μM) and shapes for LNMO (Fig. 1a–c). In contrast, LFP exhibits a more regular bean-like structure with smaller particle sizes (200 nm), as it is possible to observe in Fig. S1a. In the case of the blended powders, due to the difference in their particle sizes, the smaller LFP particles are dispersed randomly on the LNMO surface, effectively occupying the spaces or gaps between the larger and irregular LNMO particles (Fig. 1d–i).

The EDX analysis (Fig. S2) shows a better distribution of LFP particles in the sample containing a lower percentage of this material (*e.g.* 2 wt% LFP). In fact, more agglomerates are present in the mixture of material containing 10 % of LFP (Fig. S2b). This suggests that a smaller amount of LFP is better distributed through the RAM mixing process.

This particular distribution of smaller LFP particles densely packed within the interstitial spaces among the larger LNMO particles can have a significant effect on the subsequent electrode manufacturing process, resulting in a more homogeneous microstructure. For example, this microstructural configuration can improve electron and ion transport pathways within the blended material, which could potentially lead to enhanced electrochemical performances [36].

Regarding the crystalline structure, the XRD patterns of the blended electrodes align with the theoretical patterns of each single component (Fig. 1j). The XRD patterns represent an overlay of the patterns of the individual components, and the intensity of LFP signals rises proportionally with its higher mass fractions into the blend. Notably, no new phases or impurities are discerned in the blends, suggesting that the individual materials demonstrate good stability towards each other, with no evident chemical interactions or sample degradation occurring during the blending procedure.

To confirm the distribution of LFP particles and the influence on the final blended chemical-physical behaviour, the BET specific surface area (SSA) of the different samples was evaluated by means of N_2 adsorption/desorption isotherms. As illustrated in (Fig. 1k), LFP exhibits a significantly larger surface area (15.9 m^2 g^{-1}), primarily attributed to the smaller particle sizes. Conversely, pure LNMO displays a reduced surface area, approximately 1.0 m^2 g^{-1}. Concerning the blended cathodes, the introduction of LFP enhances the surface area to 1.3 m^2 g^{-1} for LNMO +2%LFP and 3.7 m^2 g^{-1} for LNMO +10%LFP. This corresponds to a 30 % increase in specific surface area for LNMO +2%LFP and a remarkable 270 % increase for LNMO +10%LFP compared to pure LNMO. The results of the surface area analysis are in good agreement with the

Table 1
Samples name according to blending percentage.

Sample name	Amount (wt.%)	
	LNMO	LFP
LNMO	100	0
LNMO + 2%LFP	98	2
LNMO +10%LFP	90	10

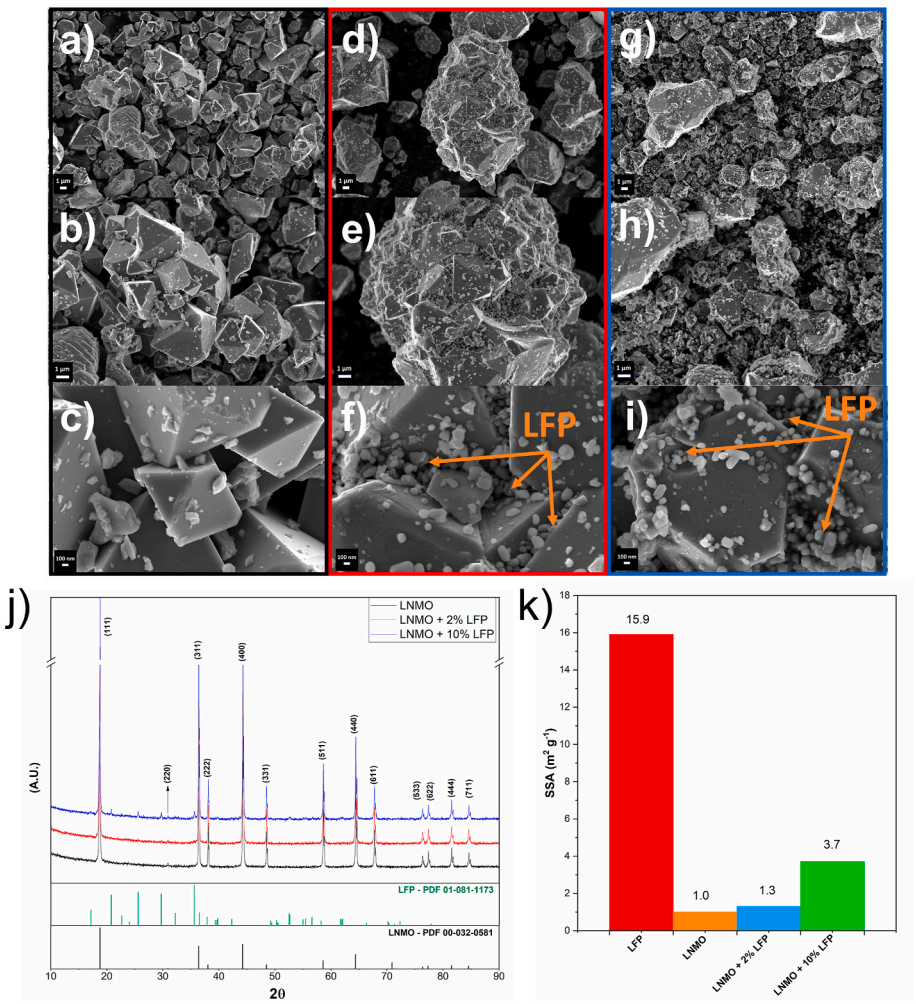

Fig. 1. FE-SEM micrographs of pure and blended cathode materials at different magnifications: pure LNMO at 2.5kX (a), 5.0kX (b), 25kX (c); LNMO + 2%LFP at 2.5kX (d), 5.0kX (e), 25kX (f); LNMO + 10%LFP at 2.5kX (g), 5.0kX (h), 25kX (i). XRD comparison of pure LNMO, LNMO +2%LFP and LNMO +10%LFP (j), SSA comparison of pure LFP, pure LNMO, LNMO + 2%LFP and LNMO +10%LFP (k).

observations from the FE-SEM micrographs, indicating a distribution of LFP particles in the electrode that can result in a different contact area between the active materials and the electrolyte.

3.2. Electrochemical characterization

3.2.1. Half cell

Considering the observations from the morphological and physical-chemical analysis of the samples, electrodes made of different materials were produced to evaluate their electrochemical properties and the role of LFP inside the cathode formulation.

For all the electrodes, the ratio of active material:carbon additive: binder was kept constant at 90:5:5 wt%, where the active material (A. M.) is pure LNMO, LNMO + 2 or 10 wt% LFP, respectively. Analogously, the areal mass loading of the electrodes was held constant at ~10.5–11.5 mg cm^{-2}.

It is important to highlight that the samples were not subjected to pressing and/or calendering processes to preserve the original porosity of the electrode. This approach aims to minimize possible limitations arising from the permeation of the electrolyte into the pores and, consequently, the transport of lithium ions [4].

The electrochemical performances of pure and blended electrodes were first investigated by cyclic voltammetry (CV) measurements in a three-electrodes cell configuration.

As it is possible to observe in Fig. S3, all LNMO-based cells exhibited discernible peaks within the investigated voltage range of 3.0–4.9 V (vs. Li/Li^+). Specifically, all samples displayed a minor peak at 4.1 V, associated with the oxidation process of manganese (Mn^{3+} to Mn^{4+}). Additionally, two partially overlapped peaks were observed in the voltage range between 4.65 and 4.75 V, corresponding to the multiple oxidations of nickel (Ni^{2+}/Ni^{3+} and Ni^{3+}/Ni^{4+}, respectively) [37].

For the blended cathode, an additional redox peak corresponding to the oxidation of iron (Fe^{2+}/Fe^{3+}) is observed, indicating that in both the blended electrodes the LFP electrochemical reaction is consistent and reversible [38]. Interestingly, the area attributable to the reversible redox process for LFP is five times greater for the blended electrode containing 10 wt% than the sample containing only 2 wt% LFP. This confirms how the capacity attributable to the LFP is directly correlated with the amount of mass added during the physical mixing.

By comparing five CV cycles for the three different samples (Figs. S3a–c), it is evident that, excluding the first cycle during which a greater polarization is observed, the profiles of the subsequent cycles overlap perfectly for both of the blended samples, especially for the one with 2 wt% LFP. In contrast, the pure LNMO electrode shows less overlapping CV profiles and a partial activation as the number of cycles increases. In general, it can be stated that the two blended cathodes show excellent stability in the investigated potential range, displaying no undesirable interaction between the two materials or the presence of unforeseen reactions.

Cyclic voltammetry at different scan rates (*i.e.* 0.1, 0.2, 0.3, 0.4 and

0.5 mV s^{-1}) over the voltage range from 3.0 to 4.9 V was carried out in the three electrodes configuration (Fig. 2) to evaluate the Li-ion insertion/extraction kinetics and the apparent diffusion coefficient through the Randles-Ševčík equation.

$$I_p = 2.69 \times 10^5 n^{3/2} A D_{Li}^{1/2} C_{Li} \nu^{1/2} \quad (1)$$

where I_p is the peak current, n is the number of electrons involved in the reaction, A is the electrode area (0.785 cm^2 in this experiment), D_{Li} is the diffusion coefficient (cm^2 s^{-1}), C_{Li} is the lithium-ion concentration (mol cm^{-3}), and ν is the scan rate (V s^{-1}).

As expected, with the increase of scan rate, the oxidation and reduction peaks become broader and less distinguishable due to the slower charge transfer in the material. Considering the difference between the values of the oxidation and reduction peaks, we selected two couples of oxidation/reduction peaks, marked as O1/R1 (related to Mn^{3+}/Mn^{4+}) and O2/R2 (related to Ni^{3+}/Ni^{4+}), as shown in Fig. 2a–c, for the D_{Li} calculation. According to the linear relationship between I_p and $\nu^{1/2}$ (shown in Fig. 2d and e), the slope of the linear fitting was used to evaluate the apparent D_{Li}, reported in Table 2. As it can be seen from the table, D_{Li} varies by an order of magnitude between the O1/R1 and O2/R2 reactions. Nevertheless, the average diffusion coefficient aligns well with values previously reported in the literature [39–42].

The three different samples exhibit a diffusion coefficient within the same order of magnitude for each individual reaction. However, it is noteworthy that the blended cathodes demonstrate a slightly higher D_{Li} for both the O1 ($Mn^{3+} \rightarrow Mn^{4+}$) and the R2 ($Ni^{4+} \rightarrow Ni^{3+}$) reactions. This suggests that the presence of LFP increases the kinetics of some reactions, depending on the state of charge or discharge of the system. Focusing on the oxidation of Mn^{3+} to Mn^{4+}, a similar behaviour was also observed calculating the apparent diffusion coefficient from GITT analysis reported and discussed below.

To better evaluate the possible effect of the presence of the LFP on the kinetics of the reactions involved at the cathode, rate capability and capacity retention measurements were performed in half-cell configuration (coin-cell 2032) using Li metal as the anode. All tests were performed within 3.0–4.9 V vs. Li/Li^+ at RT and the practical capacity considered was 140 mAh g^{-1}, based on the electrochemical characterization of pristine LNMO. Specific capacity values for all electrodes were normalized to the total mass of active material (LNMO + LFP).

Table 2
The apparent lithium diffusion coefficients calculated from CV measurements for different O/R reaction peaks.

Sample	Apparent diffusion coefficient D_{Li} (cm^2 s^{-1})			
	O1	O2	R1	R2
LNMO	4.48×10^{-12}	2.43×10^{-9}	2.02×10^{-11}	5.49×10^{-10}
LNMO + 2%LFP	5.19×10^{-12}	2.29×10^{-9}	1.76×10^{-11}	7.00×10^{-10}
LNMO +10%LFP	4.73×10^{-12}	1.94×10^{-9}	1.75×10^{-11}	8.68×10^{-10}

Initially, the influence of LFP within the cathode was evaluated in terms of the rate capability performance of the cells (Fig. 3). In principle, this was done because mixing two materials with different particle sizes could enhance the contact points among various components of the cell, including the current collector, carbon black, and, of course, the two cathode materials, as observed from FESEM images. For the rate capability test, the half-cells were charged/discharged with a constant rate of ~ C/10 for the initial three forming cycles followed by multiple cycles, discharging at various C-rates (ranging from C/10 to 5C), while charging at a fixed rate of 1C. Fig. 3c shows the discharge profiles of the three different cathodes: LNMO, LNMO +2%LFP, and LNMO +10%LFP under different current regimes. The average capacity value for each C-rate was calculated on three cells for each sample and reported in Table 3 and Fig. S4. The average data reported in Table 3 demonstrate how the specific discharge capacity is comparable between the three samples at low C-rates (*e.g.* C/10), and it gradually remains higher for the pure LNMO cathode as the C-rates increase. In fact, at high C-rates (*e.g.* 5C), the specific capacity is different for the three cathodes, in particular it is higher for the pure LNMO cathode (~110 mAh g^{-1}) followed by LNMO +2%LFP (101 mAh g^{-1}) and LNMO +10%LFP (93 mAh g^{-1}). This means that at 5C the discharge capacity is 8 % and 15 % lower for LNMO +2%LFP and LNMO +10%LFP, respectively. Concerning the discharge profiles at different C-rates for the pure LNMO and LNMO + LFP blended electrode, similar behaviour is observable at 1C (or lower C-rates). On the contrary, at 5C, a higher discharge potential

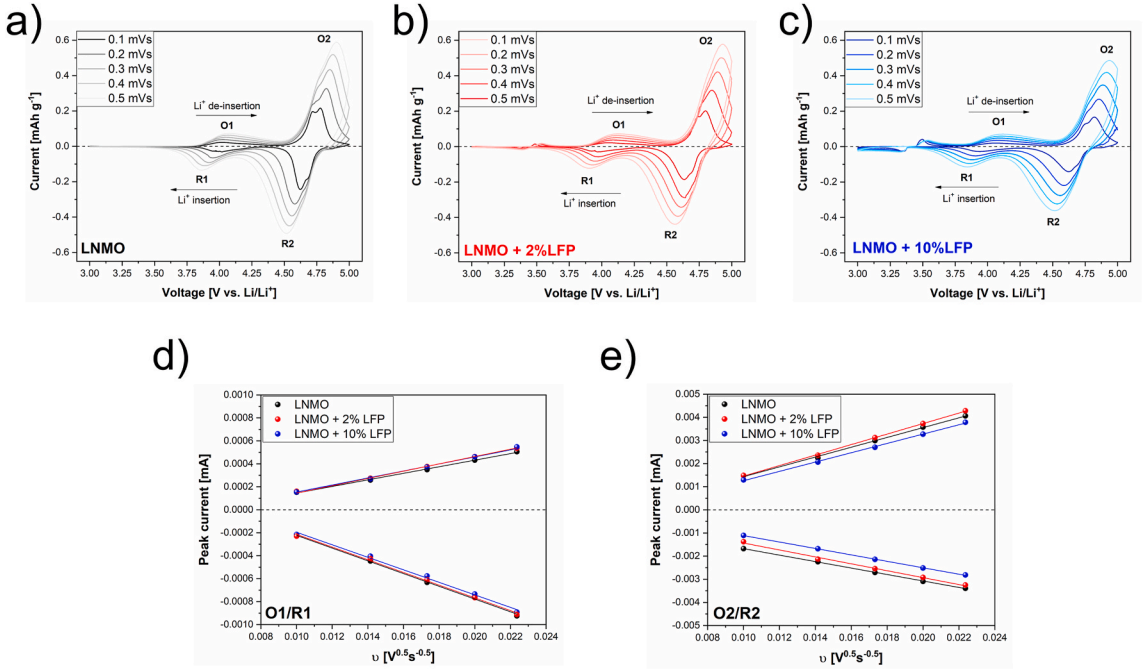

Fig. 2. Cyclic voltammetry profiles at different scan rate (0.1, 0.2, 0.3, 0.4 and 0.5 mV s^{-1}): pure LNMO (a), LNMO +2%LFP (b), LNMO + 10%LFP (c). Linear plot of the maximum current peak vs. the square root of the scan rate comparison for reaction O1 (d) and reaction O2 (e).

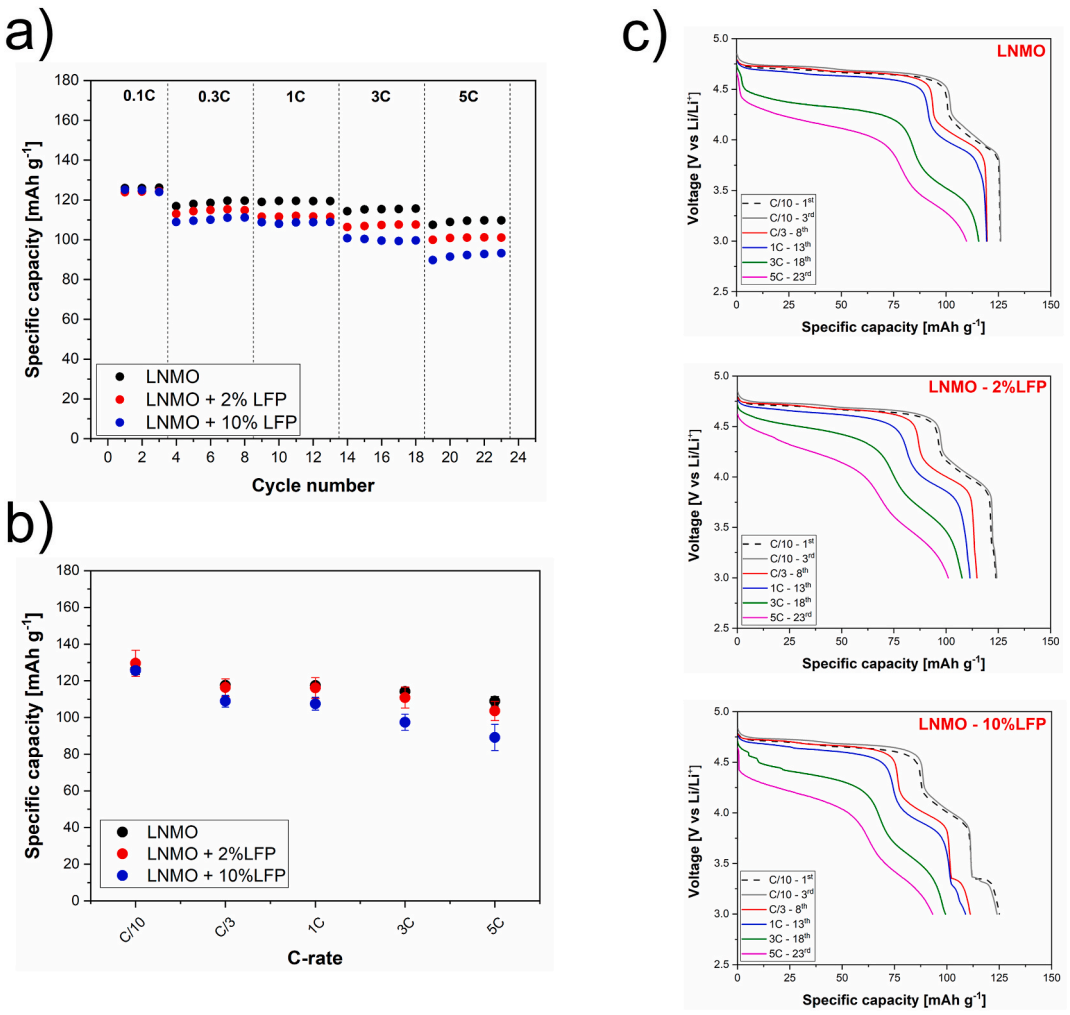

Fig. 3. Rate capability comparison of the three different cathodes (a), average discharge capacity comparison (b), discharge profiles for pure LNMO, LNMO +2%LFP, LNMO + 10%LFP.

Table 3
Values of average discharge capacity, for the rate capability test of the three different cathodes.

C-rate	Average discharge capacity, mAh g^{-1}		
	LNMO	LNMO +2%LFP	LNMO +10%LFP
C/10	126.11	129.56	125.55
C/3	117.53	116.34	108.90
1C	117.39	116.12	107.49
3C	114.14	110.83	97.43
5C	108.91	103.56	89.12

can be observed in the range between 4.5 and 3.9 V for the sample containing 2 wt%LFP, corresponding to a reduced polarization. This behaviour suggests a faster kinetics, which can be attributed to a higher current distribution and a possible charge exchange between spinel and olivine particles, as also proposed by Klein et al. [13], and for other cathode materials by Chatzogiannakis et al. [18,19]. For a better comparison, the rate capability performance of pure LFP is included in the SI (Figs. S1c–d). LFP shows a specific capacity of 150, 132, 126, 117 and 111 mAh g^{-1} at C/10, C/3, 1C, 3C and 5C respectively. In general, the pure LFP electrode shows a good rate capability and capacity retention up to 5C, with a Coulombic efficiency close to 99.5 %.

It is worth noting that, as mentioned by Liebmann et al. [5] and Chatzogiannakis et al. [18,19] the effective C-rate, applied directly to the considered material, significantly increases with the decrease in its quantity in the blended cathode formulation. Consequently, given the low percentages of LFP in our blended cathodes, the applied current on it becomes very high. For example, if we consider a current of 0.1C calculated on the entire capacity of the electrode (which is given by the sum of the LNMO and LFP capacity), and the fact that the two materials work in two distinct potential ranges so that the current is not evenly distributed between the two, the LFP present in the cathode at 2 wt% experiences an effective current of 4C, while the LFP in the 10 wt% cathode undergoes a C-rate of 0.8C. However, when one of the components has a mass fraction lower than 10 wt% in the blend, its high effective C-rates potentially cause overlapping of the characteristic redox potentials, affecting both the rate capability and the cycle stability [5].

Furthermore, the capability rates are also significantly influenced by other factors, including homogeneity, porosity, quantity, and distribution of carbon black and binder within the electrode [5]. This observation implies that not all of the LFP participates in the lithiation and de-lithiation processes and, consequently, it does not contribute fully to the reversible capacity. This is particularly true at higher C-rates (*e.g.* 2C and 5C), where the specific capacity contribution of LFP becomes indiscernible.

However, the results obtained from the rate capability test show that lithium is effectively released from LFP (even if present in low percentages), at potential lower than 3.9 V vs Li/Li^+ up to 1C, which means that it is suitable as cyclable lithium inventory. For these reasons, the

three different electrodes were cycled in half cells at a fixed current density of 1C (charge and discharge) for 1000 cycles. This analysis was done to evaluate the possible effect of LFP on the cell, using particularly stressful testing conditions, especially for traditional liquid electrolytes (charge up to 4.9 V at 1C for 1000 cycles).

Fig. 4 shows the discharge capacity comparison (normalized to the total active mass of LNMO + LFP) for the three different cathodes. As it can be seen in Fig. 4a and Table S2, the pure LNMO cathode shows higher specific capacity, confirming the results obtained in the rate capability tests. However, as the number of cycles increases, the LNMO cathode shows a progressive capacity loss. From Fig. 4a, in particular, it is possible to see that after approximately 800 cycles the LNMO blended with 2%LFP shows a greater capacity than pure LNMO. Similarly, the sample with a higher amount of LFP (*i.e.* 10 %) shows comparable or even higher capacity than pure LNMO after 1000 cycles. This trend becomes even more evident when comparing the capacity retention values of the three samples (Fig. 4b and Table 4). After 800 cycles, a noticeable decrease in the capacity retention of the LNMO cathode is observed, with a value of around 70 % at the 900th cycle. In contrast, the two blended cathodes consistently exhibit a capacity retention higher than 80 %. Moreover, the LNMO +2%LFP sample demonstrates a capacity retention higher than 80 % up to the 1000th cycle, proving to be the most stable sample with a lower capacity loss during extended cycling. To better understand the degradation phenomenon that occurs in the cell as the cycles continue, the charge/discharge profiles are shown in Fig. S5.

Observing the 5th cycle dQ/dV profiles (Fig. 4c) for all three samples, a prominent peak at around 4–4.2 V, attributable to $Mn^{3+/4+}$ redox couples, and two peaks at potentials higher than 4.6 V, attributable to $Ni^{2+/4+}$ redox couples, are visible for all the samples. An additional peak at lower potentials (<3.6 V), attributable to $Fe^{2+/3+}$, is particularly noticeable for the sample containing 10 % of LFP. Progressively, with the increase in number of cycles, a disappearance of the peak related to Fe, along with a shift of the Mn and Ni peaks toward higher potentials, is observable. A detailed analysis of the shift of the Ni pair peaks reveals that this is particularly pronounced for the pure LNMO sample. At the 1000th cycle, the oxidation peak of $Ni^{3+/4+}$ is completely eliminated at 4.9 V, and the subsequent reduction peak shows a much lower intensity for the pure LNMO sample. As reported by Höweling et al., the partial disappearance of the peak relating to nickel oxidation is due to a smaller quantity of lithium intercalated within the spinel structure [43]. This confirms a greater polarization of the pure LNMO cathode, which intensifies during cycling due to a progressive deterioration of the system, resulting in marked capacity fade.

Table 4
Values of capacity retention related to long cycling performances of pure LNMO, LNMO +2%LFP, LNMO +10%LFP using as reference the 5th cycles (1C).

Cycle number	Capacity retention (charge/discharge) % vs. 5th cycle (1 C)		
	LNMO	LNMO +2%LFP	LNMO +10%LFP
50th	102.6	103.5	102.1
100th	103.6	104.4	100.6
200th	101.3	102.7	98.2
300th	99.1	100.3	95.5
400th	98.7	99.3	93.5
500th	96.4	97.7	92.0
600th	94.6	94.8	89.5
700th	90.3	92.8	87.6
800th	86.3	91.6	83.4
900th	72.4	87.1	81.6
1000th	70.0	88.2	77.1

To better evaluate the diffusion coefficient of lithium ions and its variation as a function of the state of charge, in presence of LFP in the cathode, galvanostatic intermittent titration technique (GITT) tests were carried out.

In this case, GITT was used to calculate the apparent diffusion coefficient of lithium ions at different charging and discharging states in a half-cell set-up [44]. For this experiment, the half cells were evaluated in the voltage range between 3 and 4.9 V, imposing a current pulse of C/10 for 10 min, followed by a rest relaxation phase of 2 h. It is important to note that, for better reproducibility, the GITT was performed after three forming cycles at C/10.

As it can be seen in Fig. 5, the three samples show similar GITT profiles. However, as expected, some differences are noticeable at low potentials, where the contribution of LFP is evident, especially for the sample with 10 wt% LFP.

In fact, upon careful observation of the curves, LNMO and LNMO +2%LFP exhibit low ΔE values at lower potentials (<4 V). In contrast, the sample with a greater quantity of LFP (LNMO + 10%LFP) shows

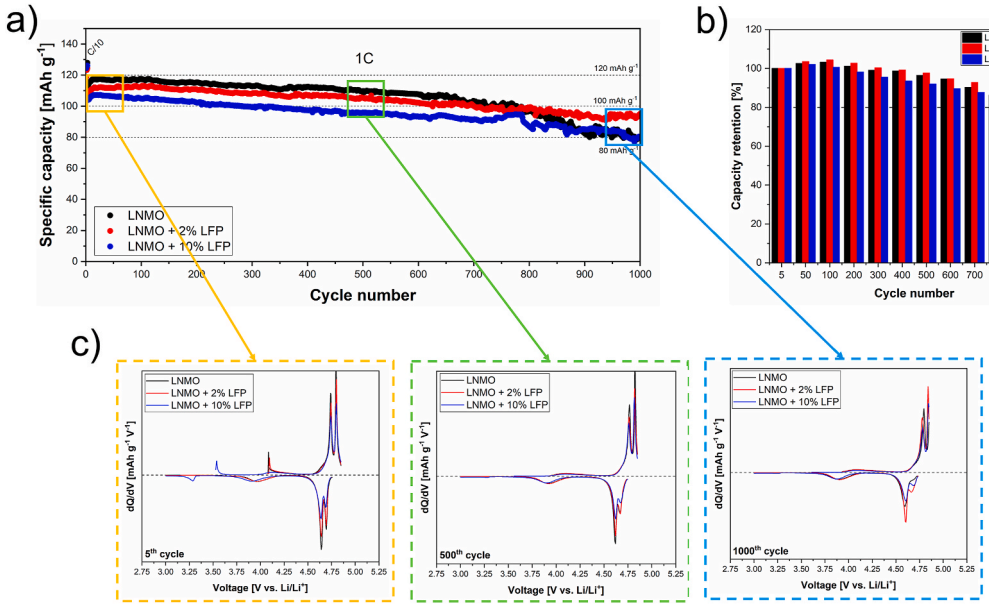

Fig. 4. Long cycling at 1C for 1000 cycles: discharge capacity comparison for pure LNMO and the two blended electrodes (a), capacity retention for different cycles, using as reference the 5th cycles (1C), dQ/dV profiles comparison for cycle 5th, 500th and 1000th (c).

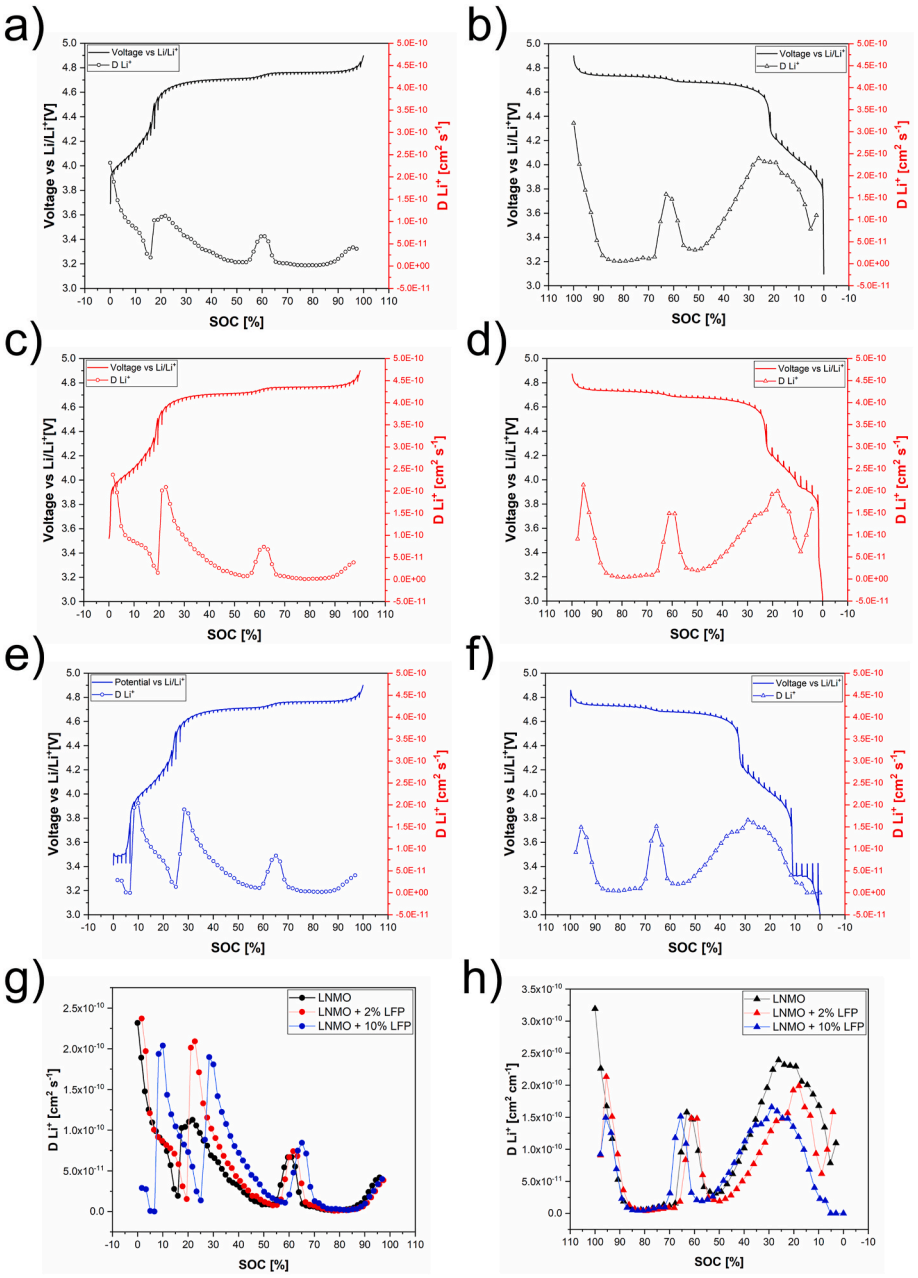

Fig. 5. Voltage vs. SOC profile and related Li^+ diffusion coefficient from GITT analysis for: pure LNMO charge (a) and discharge (b), LNMO + 2%LFP LNMO charge (c) and discharge (d), LNMO + 10%LFP LNMO charge (e) and discharge (f). D_{Li^+} values calculated from the GITT profiles as a function SOC for charge (g) and discharge (h).

more pronounced ΔE values directly correlated with the amount of olivine in the electrode. This initial profile section is followed by a region between 4 and 4.5 V, where the ΔE is more noticeable, and a third region (from 4.5 to 4.8 V), corresponding to Ni oxidation plateaus, showing low ΔE values.

The apparent diffusion coefficient was calculated directly from the GITT according to equation (2), since the high voltage spinel undergoes several two-phase reactions during lithiation [44].

$$D_{Li^+} = \frac{4}{\pi}\left(\frac{I\,V_M}{Z_A F S}\right)\left(\frac{dE_x/d_x}{dE_t/d\sqrt{t}}\right)^2, t \ll \frac{l^2}{D_{Li^+}} \quad (2)$$

where I is the applied current, V_M the molecular volume, z_A the charge of the carrier, F the Faraday constant, S the electroactive surface area, and E the voltage measured over time t and composition x.

Analysing the trend of the diffusion coefficient reveals different minima as a function of the lithium concentration in all three samples. The first minimum is observed for state of charge (SOC) < 30 %, the second for values between 30 and 60 %, and a third minimum at SOC values above 70 %. Notably the minimum values found for the diffusion coefficient shift to higher SOC values depending on the quantity of LFP present in the sample (Fig. 5c–f). As previously reported by Rahim et al. [45], the small dip in Li^+ diffusion coefficient is associated with the oxidation of Mn^{3+} to Mn^{4+} at the beginning of Li de-intercalation (low voltage) and to the oxidation of Ni^{2+}/Ni^{3+} and Ni^{3+}/Ni^{4+} at higher Li de-intercalation steps (high voltage).

The values of the diffusion coefficient of the three cathodes are comparable to each other and consistent with the ones calculated from the cyclic voltammetry analysis and with those reported in the literature (approximately with a maximum diffusion coefficient of the order of

10^{-10} cm^2 s^{-1}). Nevertheless, in a direct comparison of the diffusion coefficient values for the three samples (Fig. 5g and h), it is noticeable how the values are slightly higher for the samples containing LFP. This difference is particularly evident for SOCs between 20 and 40 % and, to a lesser extent, for SOCs between 50 and 70 %.

The slightly higher diffusion coefficients observed for the blended samples confirm a non-negligible influence of the LFP, especially at low charge states, indicating a potential interaction between the two materials as already observed for the CV tests. This interaction could be favoured by the different redox potentials at which the two cathode materials are electrochemically active. Additionally, the higher diffusion coefficient at low voltages can be directly correlated to a greater oxidation state of manganese (*i.e.*, Mn^{4+}), as previously reported in Refs. [46,47]. This aspect turns out to be non-negligible, as a higher oxidation state of manganese limits the risk of dismutation and the consequent formation of Mn^{2+}, and the leaching of this species from the LNMO structure [48,49].

In addition to GITT measurements, electrochemical impedance spectroscopy (EIS) was carried out at different states of charge (10, 50, 75 and 100 % in the potential range 3.0–4.9 V) in order to evaluate the internal resistance variation of the different cathodes. The EIS analysis was performed during the 4th cycle, after three previous forming cycles at C/10.

As shown in Fig. 6, all Nyquist plots consist of three semicircles followed by a straight diffusion line from the high to low frequency regions. The impedance plots were fitted using ZView software based on a simplified equivalent circuit (R1 + R2/CPE1 + R3/CPE2 + R4/CPE3 + W) reported in Fig. 6b. In more detail, the equivalent circuit used to fit each Nyquist plot includes an uncompensated resistance, R1, in series with three parallel R/CPE (where CPE is the constant phase element) and a Warburg element. The high-frequency resistance (R1) encompasses various contributions, including the ionic resistance of the separator and the electronic resistance of external electronic cell contacts [50]. The second resistance (R2), associated with the first semicircle at high frequencies (around 15000 Hz), primarily arises from the contact resistance between the porous electrode and the current collector [51,52]. Typically, this resistance remains nearly constant throughout the entire charging process. Still, in the high-frequency region, a second semicircle appears, and the corresponding resistance (R3) is attributed to the resistance of the passivating surface layer of the particles [53]. By moving to the mid-frequencies region, a third semicircle becomes visible, featuring a resistance (R4) attributable to charge transfer and pore resistance at the electrode/electrolyte interface, followed by a Warburg diffusion element (W) at lower frequencies, representing the Li^+ semi-infinite linear diffusion in the solid electrode [50–55].

As it can be seen from the Nyquist plot, the different semicircles overlap, making it difficult to discriminate the contributions of the single cathode materials. In particular, the charge transfer and contact resistance of the LNMO and the LFP entirely overlap, in agreement with the spectra reported in Fig. 6c–e.

The resistance values at various SOCs (10 %, 50 %, 75 %, 100 %) are reported in Table S3. At low SOC (*e.g.* 10 % and high lithium content), the total resistance of all the samples is higher than the subsequent states of charge. It is noteworthy that the presence of $LiFePO_4$ significantly increases the charge transfer resistance (R4) values at lower SOC, as

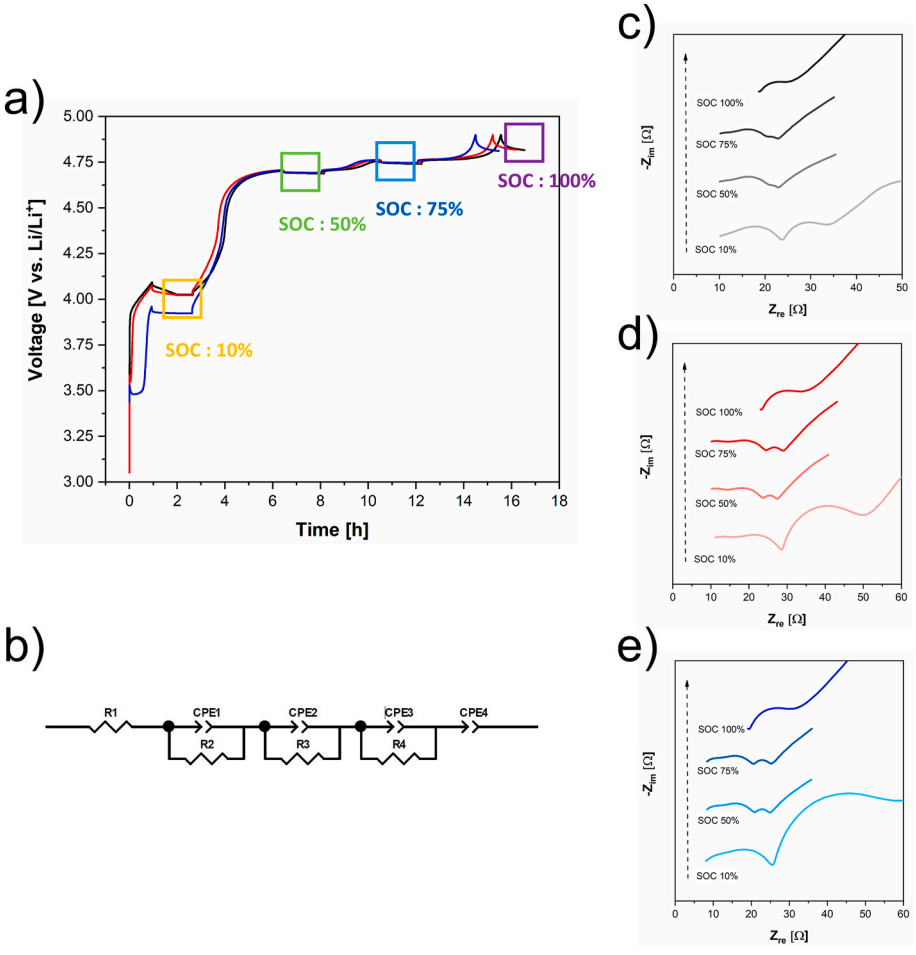

Fig. 6. Nyquist plots obtained in half-cell configuration at different states of charge (a) and equivalent circuit model used for fitting of pure LNMO (c), LNMO + 2% LFP (d), LNMO + 10%LFP (e) cathodes.

shown in Fig. 6d and e, when comparing the two blended samples with pure LNMO. As reported by Liebmann et al. when mixing materials with very different intercalation potentials, it is normal to observe a higher charge transfer resistance compared to that of the single-component electrodes [4]. However, the charge-transfer resistance diminishes as the SOC increases, particularly from 10 % to higher values (50 % or 75 %). This behaviour aligns with expectations, as the increase in SOC corresponds to an increase in potential, reaching up to 4 V, where the manganese oxidation reaction begins, resulting in a lower charge transfer resistance [56]. Similarly, the R4 remains low, approaching potentials close to 4.7 V, where the nickel oxidation reactions occur. Overall, once again, the impedance spectra confirmed that there is a contribution from the LFP, even at low quantities and low SOC (*i.e.,* lower potentials), and a more substantial contribution from the LNMO at higher SOC. At SOC 100 %, the different contributions are superimposed, therefore it is not possible to calculate the individual resistances, and only the values for R1 and R4 are reported in Table S3. More in general, a shift towards higher values for R1 and a slight increase in R4 values compared to previous SOCs is observable for all the samples.

3.2.2. Full cell

It is generally recognized that performance deterioration is more accentuated when LNMO-based electrodes are coupled with low-voltage anodes, such as graphite. In fact, in a half-cell configuration, the loss of lithium that occurs at the cathode is largely compensated by the enormous reserve of lithium present at the anode, which is metallic lithium. Therefore, to study the real effect of adding LFP to LNMO, cathodes were studied in a full cell configuration, using graphite as an anode [57].

Since the reversible capacity of the full cell is determined by the amount of active mass of LNMO in the cathode, the areal capacity of the negative electrode (graphite) was adjusted considering the one of the positive electrode in order to obtain a N/P ratio closer to 1.05–1.1. At the same time, in order not to stress the electrolyte excessively, the cells were cycled in a voltage range of 3–4.75 V at RT.

The resulting electrochemical behaviour of three different cathodes is reported in Fig. 7. By starting from the analysis of the formation cycles at C/10, the blended electrodes show a higher areal capacity, close to 1.2 mAh cm^{-2}, compared to that of pure LNMO, which shows an areal capacity of 1.05 mAh cm^{-2}. For all three samples, the Coulombic efficiency (CE) exhibits a gradual increment during the forming cycles. However, the sample with 2%LFP shows a CE of 87.4 % for the first cycle, which is higher compared to LNMO and LNMO +10%LFP, which have CEs of 82.9 % and 82.3 %, respectively. From the second cycle onward, the CE is higher for the two blended samples, with values exceeding 93 %, while LNMO shows a Coulombic efficiency lower than 86 %. At the end of the forming cycles, the CE was greater than 95 % for all samples. The lower Coulombic efficiency, already observed in half-cell, may be due to the formation of compounds such as Mn_3O_4 on the LNMO surface during the first cycles, as already observed and reported in some previous works [58,59]. However, the higher Coulombic efficiency observed for the blended cathode during the forming step suggests that the addition of LFP could effectively compensate the irreversible capacity loss.

Increasing the charge and discharge rate by an order of magnitude (*i.e.*, 1C) confirms the trend, indicating a greater capacity for the electrodes containing LFP compared to the pure LNMO sample. Both blended electrodes exhibit an areal capacity of about 1.1 mAh cm^{-2}, higher than the one observed for LNMO (0.9 mAh cm^{-2}), and a capacity retention greater than 80 % for the entire 100 cycles (calculated with respect to the 6th cycle, the first at 1C). Interestingly, the sample with a lower percentage of LFP shows a higher capacity for all the 100 cycles with a capacity retention greater than 90 % for more than 80 cycles.

Unlike half-cells, the dQ/dV profiles, derived directly from the charge/discharge curves of full cells, exhibit more complex patterns (Fig. S6). All the samples show two predominant peaks at 4.59 and 4.68 V, attributable to the double oxidation of Ni ($Ni^{2+} \rightarrow Ni^{3+} \rightarrow Ni^{4+}$). Interestingly, pure LNMO and LNMO +10%LFP samples display an additional peak at high potentials, around 4.63 V, which gradually disappears during subsequent cycles (Figs. S6a and c). According to previously published studies [60], an additional peak in the dQ/dV profile of complete LNMO/graphite cells can be attributed to electrolyte degradation. Surprisingly, the sample containing 2 wt% LFP shows no additional peaks, showing only two well-defined and overlapping peaks for all forming cycles.

By analysing the dQ/dV profiles more in detail at lower potentials (Figs. S6d–f), a broadened peak can be observed at around 3.9 V for all the samples. This peak, attributable to the manganese oxidation reaction, gradually shifts during cycling. In particular, for the pure LNMO cathode, the peak is no longer visible after two cycles. It is important to

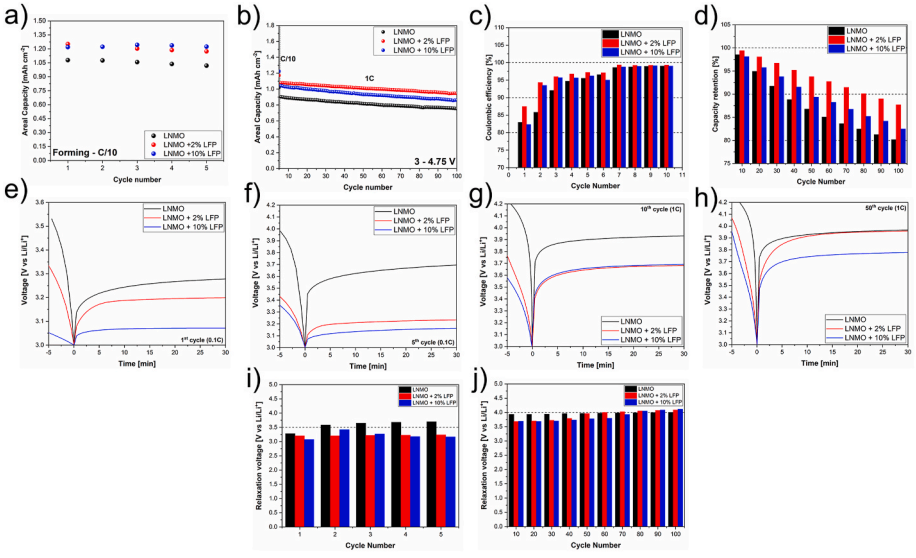

Fig. 7. Specific discharge capacity comparison for the three LNMO-based cathode in full cell configuration (using graphite as anode) in the potential range of 3–4.75 V vs. Li/Li^+, during forming cycles at C/10 (a), and for longer cycling at 1C (b). Coulombic efficiency for the first 10 cycles (c) and capacity retention up to 100 cycles, calculated with respect to the 6th cycle at 1C (d). Relaxation potential profile comparison for the three different cathodes at different cycles: 1st (e), 5th (f), 10th (g) and 50th (h). Open circuit potential (OCP) values after the rest time comparison for the firsts 5 forming cycles at C/10 (i) and for long cycling at 1C (j).

mention that the peak does not disappear, but it is simply shifted to much higher potentials (4.45 V), as it can be seen in the profiles from cycle 3 to cycle 5. On the contrary, for blended cathodes, the peak attributable to manganese is still present after several cycles. Furthermore, as the LFP content inside the cathode increases, the peak at 3.9 V undergoes a lower shift. This particular trend confirms that the presence of LFP clearly reduces the polarization of the cell. However, the distribution of LFP particles inside the cathode seems to play an important role, shielding the direct contact between LNMO particles and the electrolyte, therefore limiting the degradation of the latter.

A rest of 0.5 h is included between each cycle. This rest was included to obtain a better measure of the cell potential windows and to estimate material utilization in the absence of polarization. Fig. 7e–h displays the open circuit potential (OCP) values after the rest time for the three different cells and compares the OCP of the 1st, 5th, 10th and 50th cycles. Of course, this 0.5 h rest period could not be sufficient to reach final equilibrium for all the cells; nevertheless, this is a good compromise to estimate the equilibrium potential without contributing to significant calendar aging during cycling, as previously reported by Klett et al. [61].

In fact, from the second cycle, the relaxation potential is greater than

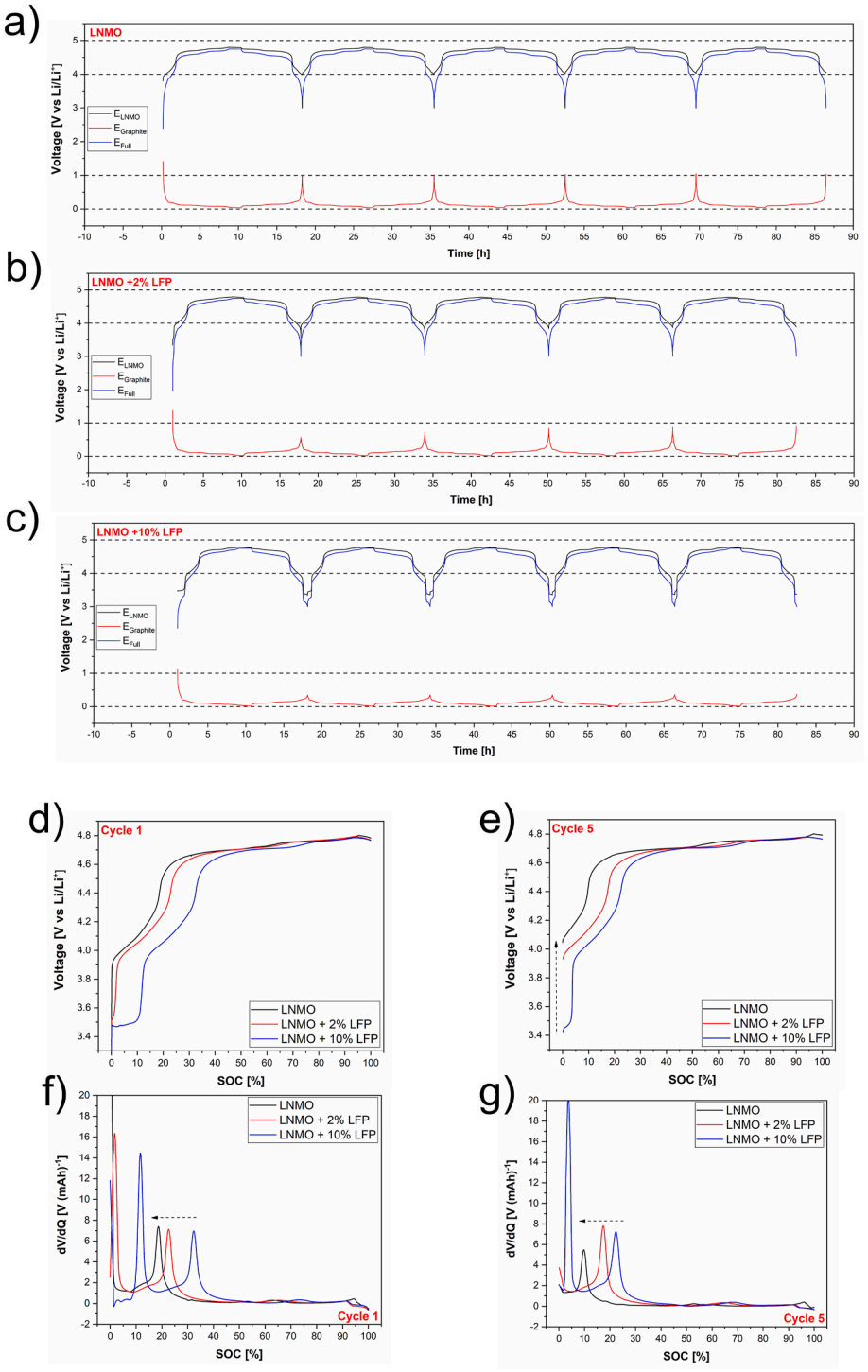

Fig. 8. LNMO-based/graphite full-cell voltage profile vs time for pure LNMO (a) LNMO + 2%LFP (b), LNMO +10%LFP (c). Voltage profiles vs SOC comparison for different cathodes for 1st (d) and 5th (e) cycle at C/10 and corresponding different voltage analysis (DVA) (f and g).

3.5 V, while for the two blended samples, it remains lower than 3.2 V after 5 cycles. When the C-rate increases (*i.e.,* 1C), the relaxation potential remains at lower values for the two blended samples for the first 50 cycles. Subsequently, an increase in the relaxation potential can be found for the sample with 2 wt%LFP until it reaches the same value as the cell with pure LNMO. On the other hand, the cell with the LNMO +10%LFP cathode takes more cycles (about 80) to reach the same relaxation potential value (Fig. 7j): this suggests that there is a clear contribution of the LFP, more visible at low C-rates and dependent on the quantity of LFP added to the cathode. In fact, the relaxation potential progressively increases during cycling, meaning that lithium is released from LFP, added to the cyclable inventory, and incrementally used to compensate the ongoing loss, probably due to progressive side-reactions and unstable SEI layer formation.

To better understand and explain the role of LFP in the cathode, three-electrode cells with lithium as a reference electrode were assembled. In this case, the voltage window of the cell was set between the cut-off voltages of 3.0 and 4.75 V, in order to evaluate the behaviour of the single electrodes (anode and cathode) during five cycles at C/10 (forming cycles). In fact, when the full cell voltage window is fixed between a defined range, both the anode and the cathode potentials change significantly during operation, as a function of the SOC of the cell [57,62–64].

As it is possible to observe from Fig. 8a–c and Fig. S7, the voltage profiles of all the cathodes reveal the typical Ni oxidation/reduction plateaus already observed in half-cell characterization. For the blended cathodes, an additional plateau is also observable in correspondence to the iron redox reaction. At the same time, the intercalation and deintercalation of lithium into/from graphite occurs in multiple stages at potential lower than 0.2 V [64].

By observing the electrodes voltage profile, a lower anode slippage is clearly visible for the cell using blended cathodes (Figs. S8a–c). During all five forming cycles, the final anode voltage (after discharge) is constantly equal or higher than 1 V. On the contrary, for the cell containing LNMO +2%LFP the anode potential is close to 0.5 V after the first cycle, with a slight increase in the subsequent cycles. Analogously, a lower and constant value of anode potential (<0.5 V) is clearly visible for the cell containing LNMO + 10%LFP. This trend confirms that the presence of LFP can limit the potential growth of graphite anode, with significant consequence on cycling stability.

Interestingly, by examining the potential profile of the fifth cycle, it is possible to notice how the pure LNMO cathode reaches a greater value for the upper cut-off voltage (Figs. S8a–c). This leads the subsequent CV step to remain at higher potentials compared to those observed for blended cathodes. Reasonably, this higher cut-off value is reached for all cycles and is more marked for higher C-rates, resulting in strong stress for the electrolyte. In fact, reaching and staying at high potential values inevitably leads to greater electrolyte degradation as the cycles proceed and consequently to an accelerated capacity fade.

For a better understanding of the cell behaviour the charge curves and the correspondent dV/dQ charge profiles of the first and fifth cycles were compared for all the three cells (Fig. 8d–g). By analysing the cathode charge profiles of blended electrodes during the first cycle, it is possible to observe that the oxidation process at low potentials exclusively involves LFP, which releases a first amount of lithium, which is consumed by the formation of the SEI layer on the graphite anode. Conversely at higher potentials, the de-lithiation of the LNMO occurs, providing the lithium necessary for the reversible charging and discharging process. In the fifth cycle it is clearly visible how the cathode potential shifts towards higher values (Fig. 8e). This is particularly evident for the pure LNMO cathode that, after 5 cycles, no longer reaches values lower than 4 V during charge and discharge. Once again, this confirms that LNMO only operates at high voltage plateau region (~4.75 V) without accessing lower voltage plateau (*i.e.,* 4 V) [62,65] and the 3 V cut-off potential, set for the full cell, is reached by the increasing of the graphite potential (over 0.8 V). This means some of the lithium is not properly de-intercalated from the graphite and is lost during SEI restoration [43].

The difference between the blended and pure LNMO cathode is particularly evident from differential voltage analysis (DVA or dV/dQ), as depicted in Fig. 8f and g. In this case, each peak corresponds to the transition from one plateau to another of the cathode, as a function of the SOC of the cell. Consequently, DVA is a useful tool to verify and compare the deterioration of cell performance. Comparing the first and fifth cycles, in correspondence with a capacity windows shrinkage, the cathode peaks get closer to each other. This behaviour of the peaks is much more marked for cells with pure LNMO, confirming an important polarization during the forming cycles. On the contrary, it can be seen how the peak shifting and intensity reduction are less marked for the blended cathodes, in particular for the sample with 2 wt% LFP.

In general, an upper cut-off potential is critical for transition metal oxide-based cathodes since capacity fade is accelerated by higher cut-off voltages [63]. In fact, as previously reported by Michalak et al. [64], when the potential of the graphite during the discharge reaches potential values equal to or greater than 0.9 V, the SEI layer is inevitably damaged. The degradation of the SEI layer involves the formation of a new reactive surface on the graphite anode, with the consequent consumption of new lithium and electrolyte during the restoration of a new SEI layer. This phenomenon is accompanied by the formation of parasitic oxidation products at the cathode side, which can accelerate the degradation of the anode through the cross-talk mechanism between the electrodes [57,61]. This progressive consumption of lithium and electrolyte causes a gradual increase in the discharge potential of both the LNMO and graphite electrodes as the cycles continue, accelerating the degradation process [64] and increasing the internal resistance of the whole cell [66].

Since the increase in the discharge potentials of the electrodes is much less marked for cells containing blended cathodes, it is evident that the presence of LFP can positively affect the stabilization of the SEI layer, mitigating the consumption of lithium and electrolyte and modifying the electrodes potential endpoints. A possible explanation for this aspect can be attributed to the formation of SEI at a significantly lower potential than 4.5 V vs Li/Li^+, and therefore distant from the potential in which secondary and harmful products originating from parasitic oxidation reactions appear [67]. At the same time, thanks to the lithium supplied by the LFP, a consistent amount of lithium can be recovered by the LNMO, ensuring higher capacity retention during cycling.

Even if the internal mechanisms and dynamics in blended cathodes are still difficult to elucidate, their electrochemical performances are strongly influenced by thermodynamics, besides simply depending on the kinetics of each component, as also recently reported in other studies with the support of operando X-ray diffraction (XRD) analysis [18,19]. In particular, the “buffer effect” of one of the blended components on the other is dictated by the effective overpotential, which is also affected by electrode-related parameters (*e.g.* particle size distribution, porosity, and tortuosity). In fact, the “buffer effect” phenomenon occurs when a current pulse is applied, causing a high flux of lithium and a consequent growing overpotential for one of the components, which makes the incorporation of lithium favorable into the other material. Therefore the thermodynamics will dictate the direction of the buffering current, according to the different operating potentials of the two blended active materials. In other words, the materials operating at high voltage will be the “lithium acceptor” during discharge while the material operating at lower voltage will be the “lithium donor”. Obviously, during the charging process, the roles of the two materials are reversed. This is what reasonably occurs when two materials operating at different potentials such as LFP and LNMO are mixed in very different ratios, as in our case. In this case, the effective current distribution (*i.e.* effective C-rate) on each material is different and strictly depends on the ratio of the blended components and it varies significantly with the SoC. These high effective C-rates, potentially cause overlapping of the characteristic

redox potentials, favoring the charge exchange between the two materials and affecting the cycle stability.

4. Conclusions

Resonant acoustic mixing is a reliable and scalable technique for the physical blending of LNMO and LFP cathode materials. In particular, mixing LNMO with small amounts of LFP (2 wt%) results in a better dispersion and distribution of the LFP with the LNMO particles, with the smaller LFP particles observed filling the voids and interstices between bigger LNMO particles or distributed directly on the LNMO surface.

Concerning the electrochemical performance of the blended cathodes, the electrochemical activity of LFP has been detectable up to 1C without negatively impacting the rate capability performance of the electrodes. However, it has been observed that the effect of LFP becomes more pronounced at lower states of charge, influencing the electrode lithium-ion diffusion coefficient and, consequently, the performance of LNMO at lower potentials (*e.g.* 4.1 V).

The most marked effect is on the capacity retention that is strongly affected by the presence of LFP, both in half-cell and full-cell configurations, and most significantly in the latter with graphite as the anode. This behaviour suggests that the use of LFP, even in small quantities, can participate directly in the redox process, showing a charge transfer with LNMO, thanks to the overpotential that arises due to the high effective C-rate to which LFP is subjected. In addition, LFP remains electrochemically active, for many cycles, acting as lithium donor for LNMO and compensating the lithium loss caused by the progressive side-reactions and unstable SEI layer formation, improving the capacity retention without compromising the energy density of the system.

Finally, the optimal distribution of particles within the electrode, combined with the mitigating effect on lithium loss inventory and electrolyte degradation, highlights the importance of finding a balance between mixing type, morphology, chemical-physical properties, and final electrochemical performance.

Therefore, LNMO/LFP blended cathode materials offer a promising solution for developing the next generation of LIBs. Through the strategic combination of these two active materials, blended cathodes can offer increased versatility and potential benefits in terms of cost and sustainability, without sacrificing electrochemical performance. This aspect is essential in applications requiring long-term durability, such as electric vehicles and stationary energy storage systems, where extended lifespan and reduced maintenance costs are required, confirming the need for further research efforts focused on the mixing and characterization of this combination of cathode materials.

CRediT authorship contribution statement

Daniele Versaci: Writing – original draft, Visualization, Validation, Supervision, Methodology, Investigation, Data curation, Conceptualization. **Roberto Colombo:** Writing – original draft, Visualization, Validation, Methodology, Investigation, Data curation. **Giorgio Montinaro:** Writing – original draft, Visualization, Validation, Investigation, Data curation. **Mihaela Buga:** Writing – review & editing, Resources, Investigation, Conceptualization. **Noelia Cortes Felix:** Writing – review & editing, Resources, Investigation, Conceptualization. **Gary Evans:** Writing – review & editing, Resources, Investigation, Conceptualization. **Federico Bella:** Writing – review & editing, Resources. **Julia Amici:** Writing – review & editing, Validation, Investigation. **Carlotta Francia:** Writing – review & editing, Visualization, Validation. **Silvia Bodoardo:** Writing – review & editing, Supervision, Funding acquisition, Conceptualization.

Declaration of competing interest

The authors declare that they have no known competing financial interests or personal relationships that could have appeared to influence the work reported in this paper.

Data availability

Data will be made available on request.

Acknowledgements

The authors kindly acknowledge for the financial support HYDRA project (Horizon 2020, grant agreement N° 875527). Daniele Versaci acknowledges support from FSE REACT-EU - PON Ricerca e Innovazione 2014–2020 program (Ministerial Decree no. 1062/2021).

Appendix A. Supplementary data

Supplementary data to this article can be found online at https://doi.org/10.1016/j.jpowsour.2024.234955.

References

[1] J. Amici, P. Asinari, E. Ayerbe, P. Barboux, P. Bayle-Guillemaud, R.J. Behm, M. Berecibar, E. Berg, A. Bhowmik, S. Bodoardo, I.E. Castelli, I. Cekic-Laskovic, R. Christensen, S. Clark, R. Diehm, R. Dominko, M. Fichtner, A.A. Franco, A. Grimaud, N. Guillet, M. Hahlin, S. Hartmann, V. Heiries, K. Hermansson, A. Heuer, S. Jana, L. Jabbour, J. Kallo, A. Latz, H. Lorrmann, O.M. Løvvik, S. Lyonnard, M. Meeus, E. Paillard, S. Perraud, T. Placke, C. Punckt, O. Raccurt, J. Ruhland, E. Sheridan, H. Stein, J.M. Tarascon, V. Trapp, T. Vegge, M. Weil, W. Wenzel, M. Winter, A. Wolf, K. Edström, A roadmap for transforming research to invent the batteries of the future designed within the European large scale research initiative BATTERY 2030+, Adv. Energy Mater. 12 (2022) 2102785 https://doi.org/10.1002/AENM.202102785.

[2] M. Armand, P. Axmann, D. Bresser, M. Copley, K. Edström, C. Ekberg, D. Guyomard, B. Lestriez, P. Novák, M. Petranikova, W. Porcher, S. Trabesinger, M. Wohlfahrt-Mehrens, H. Zhang, Lithium-ion batteries – current state of the art and anticipated developments, J. Power Sources 479 (2020) 228708, https://doi.org/10.1016/J.JPOWSOUR.2020.228708.

[3] R. Schmuch, R. Wagner, G. Hörpel, T. Placke, M. Winter, Performance and cost of materials for lithium-based rechargeable automotive batteries, Nat. Energy 3 (2018) 267–278, https://doi.org/10.1038/s41560-018-0107-2.

[4] T. Liebmann, C. Heubner, M. Schneider, A. Michaelis, Understanding kinetic and thermodynamic properties of blended cathode materials for lithium-ion batteries, Mater. Today Energy 22 (2021) 100845, https://doi.org/10.1016/j.mtener.2021.100845.

[5] T. Liebmann, C. Heubner, C. Lämmel, M. Schneider, A. Michaelis, Investigations on the effective electric loads in blended insertion electrodes for lithium-ion batteries, Chemelectrochem 6 (2019) 5728–5734, https://doi.org/10.1002/celc.201901554.

[6] H. Cui, C. Yin, Y. Xia, C. Wei, W. Jiang, J. Sun, B. Qiu, M. Zhu, Z. Liu, Synergy effects on blending Li-rich and classical layered cathode oxides with improved electrochemical performance, Ceram. Int. 45 (2019) 15097–15107, https://doi.org/10.1016/j.ceramint.2019.04.250.

[7] J. Wang, Y. Yu, B. Li, P. Zhang, J. Huang, F. Wang, S. Zhao, C. Gan, J. Zhao, Thermal synergy effect between $LiNi_{0.5}Co_{0.2}Mn_{0.3}O_2$ and $LiMn_2O_4$ enhances the safety of blended cathode for lithium ion batteries, ACS Appl. Mater. Interfaces 8 (2016) 20147–20156, https://doi.org/10.1021/acsami.6b06976.

[8] C. Heubner, T. Liebmann, M. Schneider, A. Michaelis, Recent insights into the electrochemical behavior of blended lithium insertion cathodes: a review, Electrochim. Acta 269 (2018) 745–760, https://doi.org/10.1016/j.electacta.2018.02.165.

[9] C. Cai, G.M. Koenig, Enhancing low electronic conductivity materials in all active material electrodes through multicomponent architecture, Energy Advances 2 (2023) 308–320, https://doi.org/10.1039/D2YA00269H.

[10] C. Heubner, T. Liebmann, C. Lämmel, M. Schneider, A. Michaelis, Deconvolution of cyclic voltammograms for blended lithium insertion compounds by using a model-like blend electrode, Chemelectrochem 5 (2018) 425–428, https://doi.org/10.1002/celc.201700997.

[11] C. Heubner, T. Liebmann, C. Lämmel, M. Schneider, A. Michaelis, Insights into the buffer effect observed in blended lithium insertion electrodes, J. Power Sources 363 (2017) 311–316, https://doi.org/10.1016/j.jpowsour.2017.07.108.

[12] A. Klein, P. Axmann, M. Wohlfahrt-Mehrens, Origin of the synergetic effects of $LiFe_{0.3}Mn_{0.7}PO_4$ – spinel blends via dynamic in situ X-ray diffraction measurements, J. Electrochem. Soc. 163 (2016) A1936–A1940, https://doi.org/10.1149/2.0741609jes.

[13] A. Klein, P. Axmann, M. Wohlfahrt-Mehrens, Synergetic effects of LiFe0.3Mn0.7PO4–LiMn1.9Al0.1O4 blend electrodes, J. Power Sources 309 (2016) 169–177, https://doi.org/10.1016/j.jpowsour.2016.01.093.

[14] S.B. Chikkannanavar, D.M. Bernardi, L. Liu, A review of blended cathode materials for use in Li-ion batteries, J. Power Sources 248 (2014) 91–100, https://doi.org/10.1016/j.jpowsour.2013.09.052.

[15] A.J. Smith, S.R. Smith, T. Byrne, J.C. Burns, J.R. Dahn, Synergies in blended LiMn $_2$ O $_4$ and Li[Ni $_{1/3}$ Mn $_{1/3}$ Co $_{1/3}$]O $_2$ positive electrodes, J. Electrochem. Soc. 159 (2012) A1696–A1701, https://doi.org/10.1149/2.056210jes.

[16] D. Wu, H. Ren, Y. Guo, X. Zhang, Z. Zhang, J. Li, Synergetic effects of LiNi1/3Co1/3Mn1/3O2–LiMn2O4 blended materials on lithium ionic transport for power performance, Ionics 25 (2019) 1595–1605, https://doi.org/10.1007/s11581-018-2650-z.

[17] S.K. Jeong, J.S. Shin, K.S. Nahm, T. Prem Kumar, A.M. Stephan, Electrochemical studies on cathode blends of LiMn2O4 and Li[Li1/15Ni1/5Co2/5Mn1/3O2], Mater. Chem. Phys. 111 (2008) 213–217, https://doi.org/10.1016/j.matchemphys.2008.03.032.

[18] D. Chatzogiannakis, M. Fehse, M.A. Cabañero, N. Romano, A. Black, D. Saurel, M. R. Palacin, M. Casas-Cabanas, Towards understanding the functional mechanism and synergistic effects of LiMn2O4 - LiNi0.5Mn0.3Co0.2O2 blended positive electrodes for Lithium-ion batteries, J. Power Sources 591 (2024) 233804, https://doi.org/10.1016/j.jpowsour.2023.233804.

[19] D. Chatzogiannakis, V. Arszelewska, P.-E. Cabelguen, F. Fauth, M. Casas-Cabanas, M.R. Palacin, Understanding charge transfer dynamics in blended positive electrodes for Li-ion batteries, Energy Storage Mater. 69 (2024) 103414, https://doi.org/10.1016/j.ensm.2024.103414.

[20] H.Y. Tran, C. Täubert, M. Fleischhammer, P. Axmann, L. Küppers, M. Wohlfahrt-Mehrens, LiMn2O4 spinel/LiNi0.8Co0.15Al0.05O2 blends as cathode materials for lithium-ion batteries, J. Electrochem. Soc. 158 (2011) A556, https://doi.org/10.1149/1.3560582.

[21] B. Wang, F. Jin, Y. Xie, H. Luo, F. Wang, T. Ruan, D. Wang, Y. Zhou, S. Dou, Holey graphene modified LiFePO4 hollow microsphere as an efficient binary sulfur host for high-performance lithium-sulfur batteries, Energy Storage Mater. 26 (2020) 433–442, https://doi.org/10.1016/j.ensm.2019.11.016.

[22] K.G. Gallagher, S.-H. Kang, S.U. Park, S.Y. Han, xLi2MnO3·(1−x)LiMO 2 blended with LiFePO4 to achieve high energy density and pulse power capability, J. Power Sources 196 (2011) 9702–9707, https://doi.org/10.1016/j.jpowsour.2011.07.054.

[23] C. Heubner, T. Liebmann, C. Lämmel, M. Schneider, A. Michaelis, Synergy effects in blended electrodes for Li-ion batteries: a conceptual clarification, Batter Supercaps 5 (2022), https://doi.org/10.1002/batt.202100171.

[24] J. Chen, Z. Huang, W. Zeng, F. Cao, J. Ma, W. Tian, S. Mu, Synthesis, modification, and lithium-storage properties of spinel LiNi0.5Mn1.5O4, Chemelectrochem 8 (2021) 608–624, https://doi.org/10.1002/CELC.202001414.

[25] T. Fu, D. Lu, Z. Yao, Y. Li, C. Luo, T. Yang, S. Liu, Y. Chen, Q. Guo, C. Zheng, W. Sun, Advances in modification methods and the future prospects of high-voltage spinel LiNi0.5Mn1.5O4 — a review, J Mater Chem A Mater 11 (2023) 13889–13915, https://doi.org/10.1039/D3TA01777J.

[26] D. Versaci, G. Kastrinaki, G. Ganas, D. Zarvalis, G. Karagiannakis, J. Amici, C. Francia, S. Bodoardo, Influence of electrode fabrication process on nanocrystalline tin oxide electrochemical behaviour for high voltage SnO2/LNMO full cell Li-ion battery, J. Energy Storage 65 (2023), https://doi.org/10.1016/j.est.2023.107357.

[27] J. Hu, W. Huang, L. Yang, F. Pan, Structure and performance of the LiFePO4 cathode material: from the bulk to the surface, Nanoscale 12 (2020) 15036–15044, https://doi.org/10.1039/D0NR03776A.

[28] T.-F. Yi, Y.-M. Li, X.-Y. Li, J.-J. Pan, Q. Zhang, Y.-R. Zhu, Enhanced electrochemical property of FePO4-coated LiNi0.5Mn1.5O4 as cathode materials for Li-ion battery, Sci. Bull. 62 (2017) 1004–1010, https://doi.org/10.1016/j.scib.2017.07.003.

[29] D. Liu, J. Trottier, P. Charest, J. Fréchette, A. Guerfi, A. Mauger, C.M. Julien, K. Zaghib, Effect of nano LiFePO4 coating on LiMn1.5Ni0.5O4 5V cathode for lithium ion batteries, J. Power Sources 204 (2012) 127–132, https://doi.org/10.1016/j.jpowsour.2011.11.059.

[30] W.H. Jang, M.C. Kim, S.N. Lee, J.Y. Ahn, V. Aravindan, Y.S. Lee, Enhanced elevated temperature performance of LiFePO4 modified spinel LiNi0.5Mn1.5O4 cathode, J. Alloys Compd. 612 (2014) 51–55, https://doi.org/10.1016/j.jallcom.2014.05.149.

[31] F.A. Vásquez, N.C. Rosero-Navarro, A. Miura, Y. Goto, K. Tadanaga, J.A. Calderón, Beneficial Effect of LiFePO4/C coating on Li0.9Mn1.6Ni0.4O4 obtained by microwave heating, Electrochim. Acta 437 (2023) 141544, https://doi.org/10.1016/j.electacta.2022.141544.

[32] B. Xiao, J. Liu, Q. Sun, B. Wang, M.N. Banis, D. Zhao, Z. Wang, R. Li, X. Cui, T. Sham, X. Sun, Unravelling the role of electrochemically active FePO $_4$ coating by atomic layer deposition for increased high-voltage stability of LiNi $_{0.5}$ Mn $_{1.5}$ O $_4$ cathode material, Adv. Sci. 2 (2015), https://doi.org/10.1002/advs.201500022.

[33] I.U. Khan, R. Guo, U. Farooq, S. Adhikari, H. Zhou, Parametric effects on the mixing efficiency of resonant acoustic mixing technology for high-viscosity mixture: a numerical study, Processes 11 (2023) 266, https://doi.org/10.3390/pr11010266.

[34] J.G. Osorio, F.J. Muzzio, Evaluation of resonant acoustic mixing performance, Powder Technol. 278 (2015) 46–56, https://doi.org/10.1016/j.powtec.2015.02.033.

[35] A. Vandenberg, K. Wille, Evaluation of resonance acoustic mixing technology using ultra high performance concrete, Construct. Build. Mater. 164 (2018) 716–730, https://doi.org/10.1016/j.conbuildmat.2017.12.217.

[36] Z. Mao, M. Farkhondeh, M. Pritzker, M. Fowler, Z. Chen, Charge/discharge asymmetry in blended lithium-ion electrodes, J. Electrochem. Soc. 164 (2017) A39–A47, https://doi.org/10.1149/2.0181702jes.

[37] D. Versaci, O.D. Apostu, D. Dessantis, J. Amici, C. Francia, M. Minella, S. Bodoardo, Tragacanth, an exudate gum as suitable aqueous binder for high voltage cathode material, Batteries 9 (2023) 199, https://doi.org/10.3390/batteries9040199.

[38] D.Y.W. Yu, C. Fietzek, W. Weydanz, K. Donoue, T. Inoue, H. Kurokawa, S. Fujitani, Study of LiFePO[sub 4] by cyclic voltammetry, J. Electrochem. Soc. 154 (2007) A253, https://doi.org/10.1149/1.2434687.

[39] Z. Fang, X.-L. Zhang, X.-Y. Hou, W.-L. Huang, L.-B. Li, Submicron single-crystalline LiNi0.5Mn1.5O4 cathode with modulated Mn3+ content enabling high capacity and fast lithium-ion kinetics, Rare Met. 41 (2022) 2268–2279, https://doi.org/10.1007/s12598-021-01942-7.

[40] J. Mao, M. Ma, P. Liu, J. Hu, G. Shao, V. Battaglia, K. Dai, G. Liu, The effect of cobalt doping on the morphology and electrochemical performance of high-voltage spinel LiNi0.5Mn1.5O4 cathode material, Solid State Ionics 292 (2016) 70–74, https://doi.org/10.1016/j.ssi.2016.05.008.

[41] X. Huang, K. Chen, Y. Liu, Enhancement of LiNi $_{0.5}$ Mn $_{1.5}$ O $_4$ cathode materials through interfacial modification of amorphous Al $_2$ O $_3$ in lithium ion batteries, J. Electrochem. Soc. 166 (2019) A5081–A5089, https://doi.org/10.1149/2.0141903jes.

[42] Y. Li, J. Guo, Y. Chen, S. Deng, J. Zhu, G. Cao, T. Lei, J. Zhang, S. Wang, S. Chang, Phase transition regulation and Cd-O/Cd-F compounds multi-effect modification synergistically act on LiNi0.5Mn1.5O4 cathode, Ionics 26 (2020) 1681–1693, https://doi.org/10.1007/s11581-019-03257-1.

[43] A. Höweling, S. Glatthaar, D. Nötzel, J.R. Binder, Evidence of loss of active lithium in titanium-doped LiNi0.5Mn1.5O4/graphite cells, J. Power Sources 274 (2015) 1267–1275, https://doi.org/10.1016/j.jpowsour.2014.10.199.

[44] N.M. Jobst, M. Mancini, M. Hölzle, M. Wohlfahrt-Mehrens, P. Axmann, Understanding the low-voltage behavior of stoichiometric over lithiated spinel Li $_{1+x}$ Ni $_{0.5}$ Mn $_{1.5}$ O $_4$: an electrochemical investigation, J. Electrochem. Soc. 170 (2023) 020513, https://doi.org/10.1149/1945-7111/acb8a6.

[45] A.S.A. Rahim, M.Z. Kufian, A.K.M. Arof, Z. Osman, Variation of Li diffusion coefficient during delithiation of spinel LiNi0.5Mn1.5O4, Journal of Electrochemical Science and Technology 13 (2022) 128–137, https://doi.org/10.33961/jecst.2021.00780.

[46] Y. Jiang, G. Sun, F. Yu, L. Que, L. Deng, X. Meng, Z. Wang, Surface modification by fluorine doping to increase discharge capacity of Li1.2Ni0.2Mn0.6O2 cathode materials, Ionics 26 (2020) 151–161, https://doi.org/10.1007/s11581-019-03202-2.

[47] S. Choi, J. Yoon, S. Muhammad, W.-S. Yoon, A study on the structural and electrochemical properties of Li $_{0.99}$ Ni $_{0.46}$ Mn $_{1.56}$ O $_4$ cathode material using synchrotron based in-situ X-ray diffraction, Journal of Electrochemical Science and Technology 4 (2013) 34–40, https://doi.org/10.5229/JECST.2013.4.1.34.

[48] G. Lim, D. Shin, K.H. Chae, M.K. Cho, C. Kim, S.S. Sohn, M. Lee, J. Hong, Regulating dynamic electrochemical interface of LiNi0.5Mn1.5O4 spinel cathode for realizing simultaneous Mn and Ni redox in rechargeable lithium batteries, Adv. Energy Mater. 12 (2022), https://doi.org/10.1002/aenm.202202049.

[49] J.C. Hestenes, J.T. Sadowski, R. May, L.E. Marbella, Transition metal dissolution mechanisms and impacts on electronic conductivity in composite LiNi $_{0.5}$ Mn $_{1.5}$ O $_4$ cathode films, ACS Materials Au 3 (2023) 88–101, https://doi.org/10.1021/acsmaterialsau.2c00060.

[50] J. Landesfeind, D. Pritzl, H.A. Gasteiger, An analysis protocol for three-electrode Li-ion battery impedance spectra: Part I. Analysis of a high-voltage positive electrode, J. Electrochem. Soc. 164 (2017) A1773–A1783, https://doi.org/10.1149/2.0131709jes.

[51] D. Pritzl, A.E. Bumberger, M. Wetjen, J. Landesfeind, S. Solchenbach, H. A. Gasteiger, Identifying contact resistances in high-voltage cathodes by impedance spectroscopy, J. Electrochem. Soc. 166 (2019) A582–A590, https://doi.org/10.1149/2.0451904jes.

[52] C. Bizot, M.-A. Blin, P. Guichard, P. Soudan, J. Gaubicher, P. Poizot, Aluminum current collector for high voltage Li-ion battery. Part II: benefit of the En' Safe® primed current collector technology, Electrochem. Commun. 126 (2021) 107008, https://doi.org/10.1016/j.elecom.2021.107008.

[53] F. De Giorgio, N. Laszczynski, J. von Zamory, M. Mastragostino, C. Arbizzani, S. Passerini, Graphite//LiNi0.5Mn1.5O4 cells based on environmentally friendly made-in-water electrodes, ChemSusChem 10 (2017) 379–386, https://doi.org/10.1002/cssc.201601249.

[54] J. Jang, Y.-T. Chen, G. Deysher, D. Cheng, S.-Y. Ham, A. Cronk, P. Ridley, H. Yang, B. Sayahpour, B. Han, W. Li, W. Yao, E.A. Wu, J.-M. Doux, L.H.B. Nguyen, J.A. S. Oh, D.H.S. Tan, Y.S. Meng, Enabling a Co-free, high-voltage LiNi $_{0.5}$ Mn $_{1.5}$ O $_4$ cathode in all-solid-state batteries with a halide electrolyte, ACS Energy Lett. 7 (2022) 2531–2539, https://doi.org/10.1021/acsenergylett.2c01397.

[55] S.A.J.A. Al-Hail, M.R. Amin, R.K. Petla, U. Nisar, R. Essehli, S. Ahzi, I. Belharouak, Understanding the nature of capacity decay and interface properties in Li//LiNi $_{0.5}$ Mn $_{1.5}$ O $_4$ cells by cycling aging and titration techniques, ACS Appl. Energy Mater. 3 (2020) 6400–6407, https://doi.org/10.1021/acsaem.0c00614.

[56] H. Duncan, Y. Abu-Lebdeh, I.J. Davidson, Study of the cathode–electrolyte interface of LiMn[sub 1.5]Ni[sub 0.5]O[sub 4] synthesized by a sol–gel method for Li-ion batteries, J. Electrochem. Soc. 157 (2010) A528, https://doi.org/10.1149/1.3321710.

[57] M.D. Levi, V. Dargel, Y. Shilina, V. Borgel, D. Aurbach, I.C. Halalay, Tailoring the potential window of negative electrodes: a diagnostic method for understanding parasitic oxidation reactions in cells with 5 V LiNi0.5Mn1.5O4 positive electrodes, J. Power Sources 278 (2015) 599–607, https://doi.org/10.1016/j.jpowsour.2014.12.130.

[58] M. Lin, L. Ben, Y. Sun, H. Wang, Z. Yang, L. Gu, X. Yu, X.-Q. Yang, H. Zhao, R. Yu, M. Armand, X. Huang, Insight into the atomic structure of high-voltage spinel LiNi $_{0.5}$ Mn $_{1.5}$ O $_4$ cathode material in the first cycle, Chem. Mater. 27 (2015) 292–303, https://doi.org/10.1021/cm503972a.

[59] N.R. Park, Y. Li, W. Yao, M. Zhang, B. Han, C. Mejia, B. Sayahpour, R. Shimizu, B. Bhamwala, B. Dang, S. Kumakura, W. Li, Y.S. Meng, Understanding the role of

lithium borate as the surface coating on high voltage single crystal LiNi $_{0.5}$ Mn $_{1.5}$ O $_{4}$, Adv. Funct. Mater. (2023), https://doi.org/10.1002/adfm.202312091.
[60] F. Zou, H.C. Nallan, A. Dolocan, Q. Xie, J. Li, B.M. Coffey, J.G. Ekerdt, A. Manthiram, Long-life LiNi0.5Mn1.5O4/graphite lithium-ion cells with an artificial graphite-electrolyte interface, Energy Storage Mater. 43 (2021) 499–508, https://doi.org/10.1016/j.ensm.2021.09.033.
[61] M. Klett, J.A. Gilbert, S.E. Trask, B.J. Polzin, A.N. Jansen, D.W. Dees, D. P. Abraham, Electrode behavior RE-visited: monitoring potential windows, capacity loss, and impedance changes in Li $_{1.03}$ (Ni $_{0.5}$ Co $_{0.2}$ Mn $_{0.3}$) $_{0.97}$ O $_{2}$/ Silicon-Graphite full cells, J. Electrochem. Soc. 163 (2016) A875–A887, https://doi.org/10.1149/2.0271606jes.
[62] J.-H. Kim, N.P.W. Pieczonka, Z. Li, Y. Wu, S. Harris, B.R. Powell, Understanding the capacity fading mechanism in LiNi0.5Mn1.5O4/graphite Li-ion batteries, Electrochim. Acta 90 (2013) 556–562, https://doi.org/10.1016/j.electacta.2012.12.069.
[63] W.M. Dose, C. Xu, C.P. Grey, M.F.L. De Volder, Effect of anode slippage on cathode cutoff potential and degradation mechanisms in Ni-rich Li-ion batteries, Cell Rep Phys Sci 1 (2020) 100253, https://doi.org/10.1016/j.xcrp.2020.100253.
[64] B. Michalak, B.B. Berkes, H. Sommer, T. Brezesinski, J. Janek, Electrochemical cross-talk leading to gas evolution and capacity fade in LiNi $_{0.5}$ Mn $_{1.5}$ O $_{4}$/graphite full-cells, J. Phys. Chem. C 121 (2017) 211–216, https://doi.org/10.1021/acs.jpcc.6b11184.
[65] B. Aktekin, M.J. Lacey, T. Nordh, R. Younesi, C. Tengstedt, W. Zipprich, D. Brandell, K. Edström, Understanding the capacity loss in LiNi $_{0.5}$ Mn $_{1.5}$ O $_{4}$ –Li $_{4}$ Ti $_{5}$ O $_{12}$ lithium-ion cells at ambient and elevated temperatures, J. Phys. Chem. C 122 (2018) 11234–11248, https://doi.org/10.1021/acs.jpcc.8b02204.
[66] S. Krueger, R. Kloepsch, J. Li, S. Nowak, S. Passerini, M. Winter, How do reactions at the anode/electrolyte interface determine the cathode performance in lithium-ion batteries? J. Electrochem. Soc. 160 (2013) A542–A548, https://doi.org/10.1149/2.022304jes.
[67] G. Gabrielli, M. Marinaro, M. Mancini, P. Axmann, M. Wohlfahrt-Mehrens, A new approach for compensating the irreversible capacity loss of high-energy Si/C| LiNi0.5Mn1.5O4 lithium-ion batteries, J. Power Sources 351 (2017) 35–44, https://doi.org/10.1016/j.jpowsour.2017.03.051.